Acta Materialia 249 (2023) 118825

Contents lists available at ScienceDirect

Acta Materialia

journal homepage: www.elsevier.com/locate/actamat

Full length article

Formation mechanisms of coprecipitates in Inconel 718 Superalloys

Hariharan Sriram [a], Semanti Mukhopadhyay [a], Kamalnath Kadirvel [a], Rongpei Shi [b], Michael J. Mills [a], Yunzhi Wang [a,*]

[a] Department of Materials Science and Engineering, The Ohio State University, Columbus, OH 43210, United States
[b] School of Materials Science and Engineering, Harbin Institute of Technology, Shenzhen 518055, China

A B S T R A C T

Recent experimental observations have shown various γ' / γ'' coprecipitate microstructures in Inconel 718-based alloys. Although their growth and coarsening behaviors have been investigated recently, the heterogeneous nucleation mechanisms of γ'' precipitates on pre-existing γ' precipitates that lead to the formation of these coprecipitates are yet to be understood. In this study, we use primarily phase field simulations to analyze the individual and combined effects of concentration and coherency stress fields associated with a growing γ' precipitate at different sizes on heterogeneous nucleation of γ'' on the surfaces of the γ' particle and the coprecipitate configurations formed. The chemical driving force for nucleation is obtained from a pseudo-ternary database calibrated against the latest CALPHAD databases for Ni-base superalloys. At the same time, contributions from elastic interaction and anisotropic interfacial energy of the γ' / γ'' interface are quantified. Subsequently, a statistical analysis based on the classical nucleation theory is combined with the phase field simulations to understand the nucleation events leading to various coprecipitate configurations. Our analyses, for the first time, indicate that the choice between the formation of compact and sandwich-like coprecipitates is determined by the size of γ' before the first nucleation event of γ'', interfacial energies between the γ, γ' and γ'' phases, and the solute depletion zone around a growing γ' precipitate.

1. Introduction

The Natural Gas-fired Combined-Cycle (NGCC) powerplants emit significantly less CO_2 when compared to the coal-fired powerplants. According to the U.S. Energy Information Administration, the annual capacity of NGCC power generation has increased from about 100 Gigawatts in 2002 to 264 Gigawatts by 2018 [1]. To further increase the efficiency of NGCC power plants, gas turbines must have higher firing temperatures and pressure ratios. One major bottleneck in realizing the design goals is the lack of turbine disk materials that can operate safely at 650 ℃ and bear stresses of magnitude over 690 MPa.

The current disk materials, such as Inconel 718 and 625, are strengthened by metastable γ'' precipitates. These precipitates begin to coarsen rapidly when exposed to a temperature above 620 °C. Additionally, the γ'' precipitates transform into a thermodynamically stable δ phase at higher temperatures [2]. These phenomena render these materials incapable of safe operation at higher temperatures. One possible alternative would be to use γ' strengthened alloys currently used in jet engine disks (such as R88DT and U720) [3] that operate at much higher temperatures. However, the large sizes and thicknesses of land-based turbine disks make the component experience slow-cooling rates during heat treatment, and the γ' precipitates are susceptible to significant over-ageing when processed through slow cooling [4]. These difficulties call for a new approach to developing a coarsening-resistant γ'-strengthened Ni-based superalloy that can be slowly cooled.

The widely used Inconel 718 alloy consists of two major intragranular precipitate phases – γ' ($L1_2$, cubic) and γ'' (DO_{22}, tetragonal). The γ'' is a metastable phase composed of Ni_3Nb [5,6]. The coherent disk-shaped precipitates maintain the following orientation relationship with the matrix γ (FCC) phase $-\{100\}_{\gamma''}//\{100\}_{\gamma}$ and $<100>\gamma''//<100>\gamma$. Three variants with different {100} habit planes are observed. The γ' phase is composed of $Ni_3(Al,Ti)$. The γ' precipitates maintain a cube-on-cube orientational relationship with the γ matrix and generally assume either a spherical or a cuboidal shape [5] depending on the lattice misfit. In commercial Inconel 718, both γ' and γ'' precipitate out at around the same time as individual particles upon cooling. Cozar and Pineau [7] showed that modifying the alloy composition of Inconel 718, mainly Al, Nb, and Ti contents, can induce a delay in γ'' precipitation. This delay gave rise to a wide variety of coprecipitates (i.e., γ'' particles nucleate heterogeneously on the surfaces of γ' particles or vice versa). Some of the commonly observed coprecipitate configurations are presented in Fig. 1, which could be characterized as "compact" coprecipitate (Fig. 1(a)), where all six faces of a

* Corresponding author.
E-mail address: wang.363@osu.edu (Y. Wang).

https://doi.org/10.1016/j.actamat.2023.118825
Received 21 November 2022; Received in revised form 10 February 2023; Accepted 1 March 2023
Available online 4 March 2023

cuboidal γ' are coated with γ'' precipitates, "sandwich" coprecipitates (Fig. (1b)) where any two opposite faces of γ' are coated with γ'', and single lobed coprecipitates where only one of the six faces {001} are coated with γ'' (Fig. (1d) – some of the small tertiary precipitates). Among these coprecipitate configurations, the compact one showed exceptional thermal stability when exposed to temperatures well above 650 °C [7,8]. A recent study by Detor et al. [9] showed that it is possible to achieve compact coprecipitates even by slow cooling from the homogenization temperature.

Shi et al. [10] used the Multi-Phase Field (MPF) model to investigate the growth of the compact and sandwich coprecipitates. Since the study's primary goal was to analyze the growth and coarsening behaviors, it started with pre-existing coprecipitate configurations and monitored their growth and coarsening. The significant growth and coarsening resistance ability of the coprecipitates was attributed to the hard impingement between γ' and γ'', soft impingement of γ'' on adjacent faces, and reduced diffusivities of γ' stabilizers through the coated γ'' shells. However, the nucleation processes leading to the formation of different coprecipitate configurations are yet to be explored. Knowledge of the nucleation mechanisms would help optimize alloy compositions and design heat treatment schedules to achieve desired coprecipitate microstructures. More recent studies (personal communication) show that it is possible to engineer microstructure with bimodal distributions of γ' with compact coprecipitates as the secondary population and sandwich-like coprecipitates as the tertiary population (Fig. 1d). Such bimodal distribution of coprecipitates could improve the creep performance [11].

Based on previous studies, we see that several factors may influence the formation of different coprecipitate configurations. Modifying the alloy composition of Inconel 718 by systematically increasing the (Ti+Al)/Nb ratio while keeping the concentration of other alloying elements constant, the morphology changes from monolithic γ' and γ''

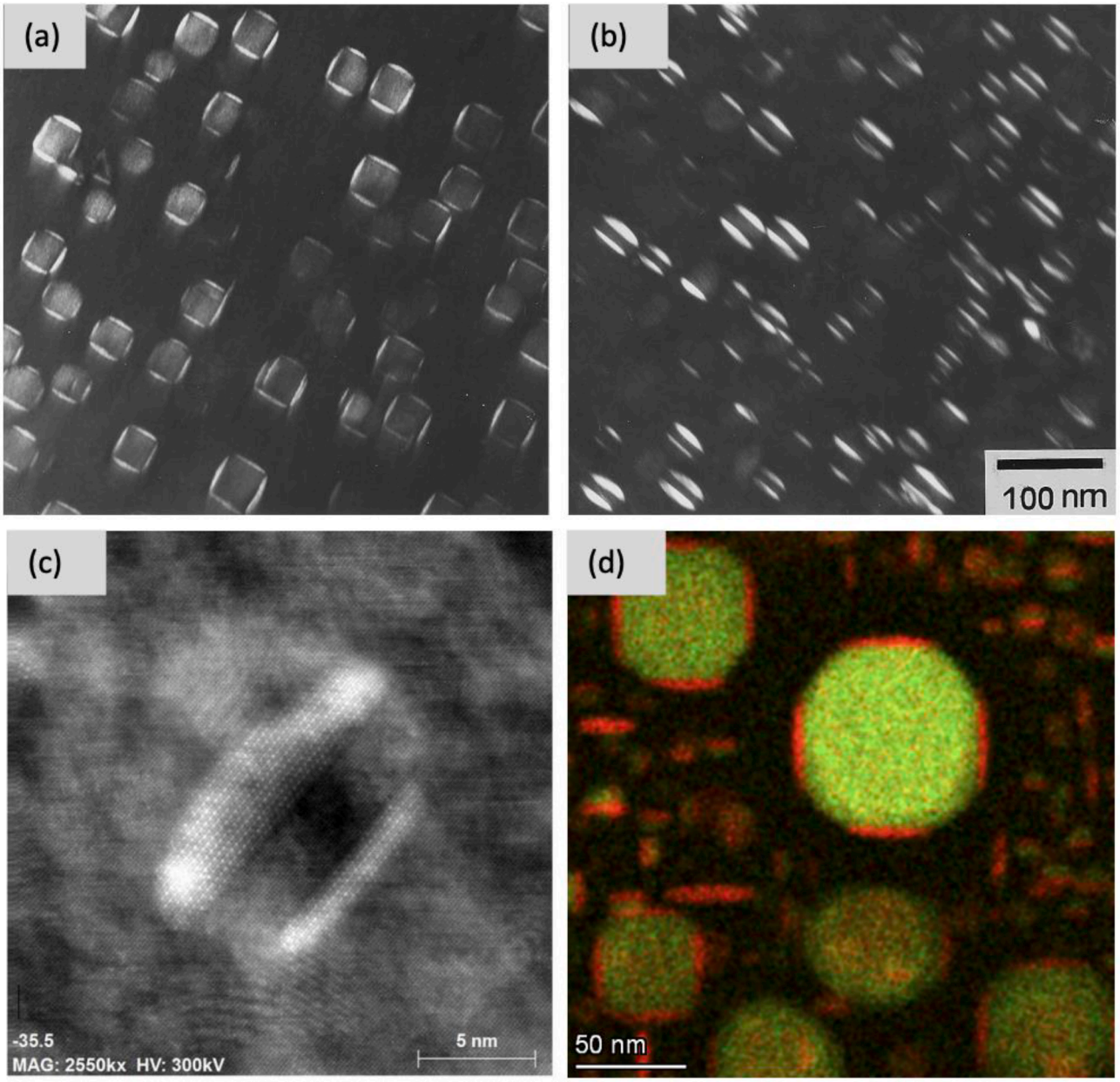

Fig. 1. Experimental characterization of various coprecipitate morphologies observed in Inconel 718 type systems (a) compact coprecipitates where all six faces of cubical γ' are coated with γ'', (b) sandwich coprecipitates where γ' is coated with γ'' on adjacent phases (reproduced with permission) [8], (c) TEM micrograph of sandwich coprecipitate where the size of γ'' is asymmetrical[33] and (d) a bimodal microstructure showing the presence of both compact and sandwich coprecipitates

precipitates to a sandwich to compact coprecipitates [7]. Ageing at higher temperatures resulted in a microstructure populated with compact coprecipitates, while lower temperatures resulted in sandwich coprecipitates [8]. The interfacial energies between different phases may also impact the formation of different coprecipitate configurations. For example, He et al. [8] reported that the interfaces between γ' and γ'' are extraordinarily flat (Fig. 2) and have a perfect atomic registry on both sides. The highly anisotropic interfacial energy between γ' /γ'' could have a significant impact on heterogeneous nucleation of γ'' on existing γ'.

In this paper, we employ a combination of the MPF model and Classical Nucleation Theory (CNT) to analyze the factors mentioned above regarding the nucleation of γ'' and the growth kinetics of γ' involved in the early stage of coprecipitate formation. The analysis is used to derive the activation energy barrier for heterogeneous nucleation of γ'' on {100} faces of γ' as a function of γ' size. The Explicit Nucleation Algorithm (ENA) [12–14], which is well suited for multi-precipitate simulations, is used to study the nucleation phenomena within the phase field framework. The stochastic nature of nucleation is lost when ENA is used for single-particle analysis. Thus, we formulate a hybrid algorithm to characterize the nucleation events based on the concept of ENA. The statistical analysis predicts the probability of forming different coprecipitate configurations for a given alloy composition.

The rest of the paper is organized as follows. The formulation of the three-dimensional (3D) MPF model and the algorithm for statistical analysis of nucleation events are presented in Section 2. In Section 3, the local concentration and elastic field associated with a growing γ' precipitate are calculated using the MPF model. They are used as an input for CNT to calculate the activation energy barrier for γ''. Subsequently, results from the statistical analysis to predict the coprecipitate morphology are presented. Key factors that influence the nucleation mechanisms and their subsequent evolution are discussed in Section 4. Additionally, coprecipitate morphologies with γ'' as the core and strategies to formulate microstructure maps based on the analysis are presented in Section 4. Limitations of the model are discussed in Section 5. The main insights derived from this study are summarized in Section 6.

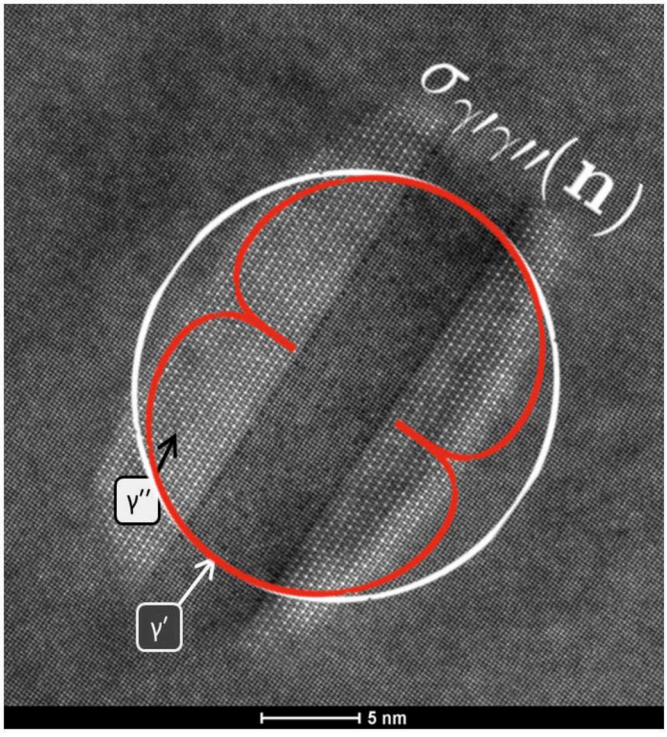

Fig. 2. TEM micrograph showing a sandwich coprecipitate [33] embedded with a Wulff plot generated by anisotropic interfacial energy formulation.

2. Methods

2.1. Multi-phase field model for coprecipitation study

The MPF model is a generalized continuum approach to treat multiple coexisting phases that can interact at higher-order junctions [15, 16]; this attribute of the model makes it an ideal candidate for studying the formation and growth of coprecipitates. The equilibrium state of triple junctions using the MPF model was investigated by Guo et al. [17] where it was found that the system converged to the static solution described by the Young's law. The phase field formulation begins with the construction of a free energy functional. For a system containing $i = 1, 2 \ldots N$ phases and $j = 1, 2 \ldots M$ elements, the total free energy functional can be expressed as the summation of three distinctively different terms, the local chemical energy f^{chem}, the gradient energy density f^{grad} and the elastic energy E^{el}:

$$F(\{\phi_i\},\{c_i\}) = \int d\mathbf{r}\ \left\{ f^{grad}(\{\phi_i\}) + f^{chem}(\{\phi_i\},\{c_i\}) \right\} + E^{el} \tag{1}$$

where ϕ_i is the i^{th} phase's structural order parameter varies smoothly from 0 to 1 across a phase boundary and c_i is the local concentration of the i^{th} element. This paper uses five structural order parameter fields to track the spatial distribution of γ, γ' and the three variants of γ''. Anti-phase domains of the ordered phases are ignored. ϕ_1 and ϕ_2 are used to represent γ and γ' phases, respectively. The three γ'' variants with their habit planes parallel to (100), (010), and (001) are represented by ϕ_3, ϕ_4 and ϕ_5, respectively. In the MPF model, these structural order parameters satisfy the following constraint at each grid point, $\sum_{\alpha=1}^{N} \phi_\alpha = 1$. For simplicity, a pseudo-ternary thermodynamic database developed by CompuTherm LLC (private communication) was used to describe the bulk chemical free energy. For each phase, the free energy density is approximated by a parabolic function, using the second derivatives of the Gibbs free energy with respect to Al and Nb concentrations at equilibrium calculated by using the database as the parabolic coefficients. The bulk chemical free energy of the system formulated in this way reads

$$f^{chem}(\{\phi_i\},\{c_i\}) = \sum_{\alpha=1}^{N} \phi_i(x) f_i(c_i(x)) \tag{2}$$

The free energy of the individual phases, f_α, is approximated by a parabolic function similar to the scheme employed in [10] and is presented below

$$f_\alpha = V_m^{-1}\left(C_{Al}\left(c_{Al}^{\alpha} - ce_{Al}^{\alpha}\right)^2 + C_{Nb}\left(c_{Nb}^{\alpha} - ce_{Nb}^{\alpha}\right)^2 \right) \tag{3}$$

where

$$C_{Al} = \frac{1}{2}\frac{\partial^2 f^{\gamma}}{\partial (c_{Al}^{\alpha})^2} = 4.2{*}10^5\ J \Big/ mol$$

and

$$C_{Nb} = \frac{1}{2}\frac{\partial^2 f^{\gamma}}{\partial (c_{Nb}^{\alpha})^2} = 5.4{*}10^5\ J \Big/ mol$$

The equilibrium concentrations of Al and Nb in γ, γ' and γ'' phases are presented in Table 1. The pseudo-ternary Ni-Al-Nb system mimics the thermodynamic properties of Inconel 718. It is calibrated to capture qualitative changes in the chemical driving force of nucleation as a function of alloy composition predicted by the complete PanNi2020

Table 1
Equilibrium composition of phases obtained from pseudo-ternary database.

Phase	Al (at%)	Nb (at%)
γ	3.62	6.8
γ'	12.8	10.6
γ''	0.9	22.6

database. The parallel tangent construction is used to calculate chemical driving force for nucleation and the nucleus composition. The driving force is calculated using the following expression that was derived for the parabolic free energy approximations

$$G_v^{chem} = \frac{2}{V_m}\left[\sum_{i=Al,Nb} C_i(c_i - c_i^{\gamma})(c_i^{\gamma''} - c_i^{\gamma})\right] \quad (4)$$

A comparison between the driving forces predicted by the pseudo-ternary and complete databases at 720°C is presented in Fig. 3.

For simplicity, the gradient energy density is formulated as a function of the structural order parameters only

$$f^{grad}(\{\phi_i\}) = \sum_{i=1}^{N}\sum_{j>i}^{N}\left[\frac{\kappa_{ij}\gamma(n_{ij})}{2}\nabla\phi_i.\ \nabla\phi_j + \omega_{ij}\ \gamma(n_{ij})|\phi_i\phi_j|\right] \quad (5)$$

where κ_{ij} and ω_{ij} are related to the interface energy σ_{ij} and interfacial width Λ_{ij} in such a manner that $\sigma_{ij} \propto \sqrt{\kappa_{ij}\omega_{ij}}$ and $\Lambda_{ij} \propto \sqrt{\kappa_{ij}/\omega_{ij}}$. To capture inter-phase interfacial energy anisotropy (for interfaces between the γ' and γ'' phases), both κ_{ij} and ω_{ij} are further multiplied by $\gamma(\mathbf{n})$, a function of the local interface normal, **n**. Such a treatment of interfacial energy anisotropy guarantees a constant boundary width for different interfacial segments [18]. For a single low-energy face parallel to the (001)γ plane (i.e., the habit plane of the 3rd variant of the γ'' phase), $\gamma(\mathbf{n}) = \left(1 + \varepsilon(n_x^2 + n_y^2)^{\frac{1}{4}}\right)\Big/(1+\varepsilon)$, where n_x, n_y and n_z are components of the unit vector **n** along the *x*, *y* and *z* directions, respectively, which are parallel to the <001> cubic directions of the γ phase. ε is the anisotropy factor, and its value is tuned to capture the TEM observed γ'' shape (Fig. 2). There is a strong cusp at the polar plot of the interfacial energy as a function of interface inclination, **n**, along the $<001>_\gamma$ directions, which gives rise to γ'/γ'' interfaces parallel to the $\{001\}_\gamma$ planes. Interfaces between the γ' phase and the 1st & 2nd variants of the

Table 2
Interfacial energies between phases used in this study.

Phase	Interfacial Energy (mJm^{-2})
γ'/γ (Isotropic)	50
γ''/γ (Isotropic)	100
γ'/γ'' (Anisotropic)	Max 125 – Min 25
γ''/γ'' (Isotropic)	150

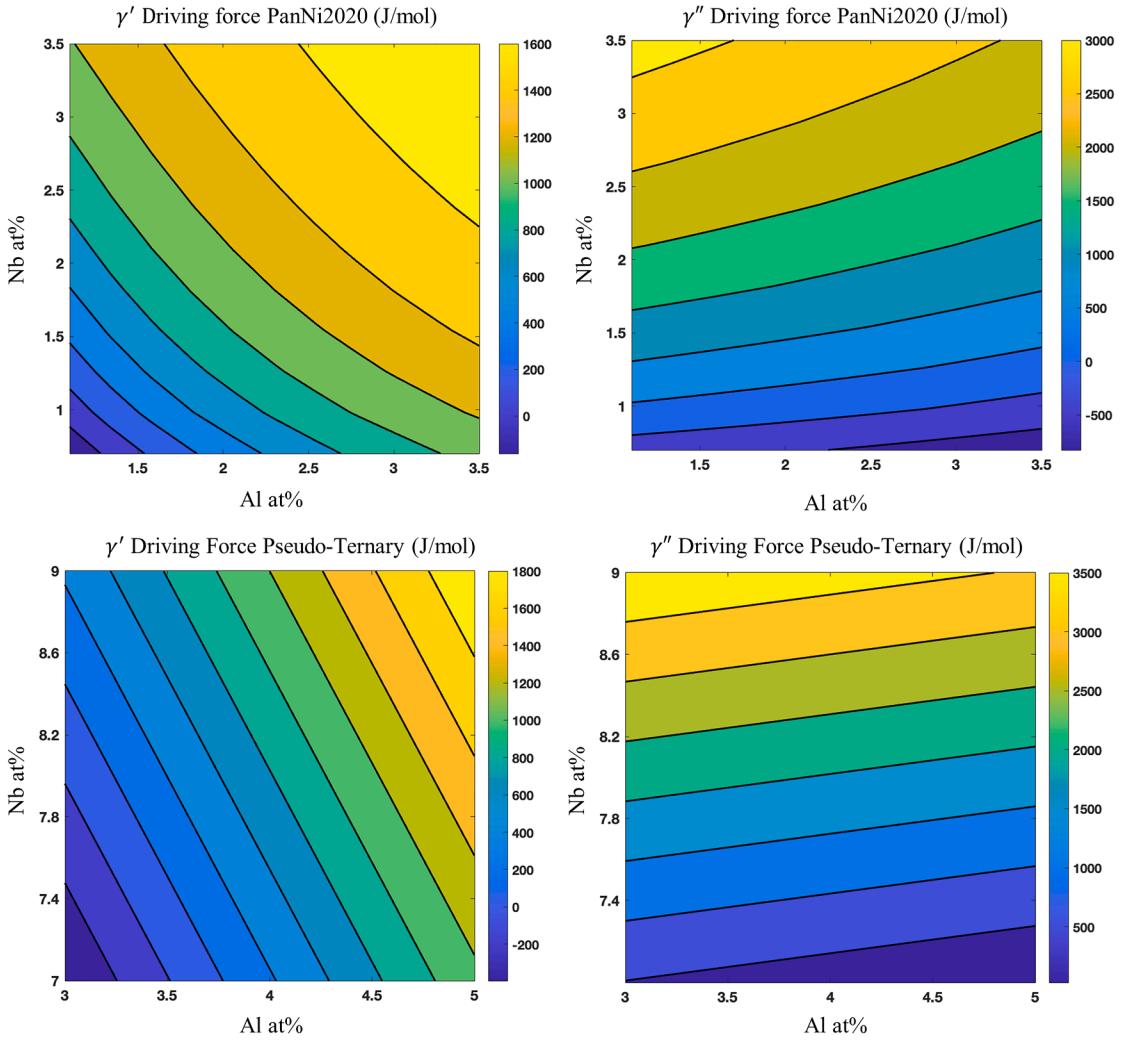

Fig. 3. Comparison of the chemical driving force of nucleation for the formation of γ' and γ'' precipitates at 720°C(Pseudo-Ternary vs. PanNi2020 database)

γ'' phase are described by analogous functions. The interfacial energies between various phases used in this study are summarized in Table 2. We have adopted the interfacial energies from Shi et al. [10]. For the γ'/γ interfaces, we have assumed the interfacial energy at the cusp to be 25 mJm^{-2}, which is the lowest among all the interfacial energies.

The coherency elastic strain energy, E^{el}, is formulated according to Khachaturyan's microscopic elasticity theory [19]. The key inputs in the formulation of E^{el}, the stress-free transformation strains (SFTS) of each phase, $\epsilon^*(i)$, are formulated as follows [10]:

$$\epsilon^*(1) = \begin{bmatrix} 0 & & \\ & 0 & \\ & & 0 \end{bmatrix}; \quad \epsilon^*(2) = \begin{bmatrix} -0.3\% & & \\ & -0.3\% & \\ & & -0.3\% \end{bmatrix};$$

$$\epsilon^*(3) = \begin{bmatrix} 2.86\% & & \\ & 0.67\% & \\ & & 0.67\% \end{bmatrix}; \quad \epsilon^*(4) = \begin{bmatrix} 0.67\% & & \\ & 2.86\% & \\ & & 0.67\% \end{bmatrix};$$

$$\epsilon^*(5) = \begin{bmatrix} 0.67\% & & \\ & 0.67\% & \\ & & 2.86\% \end{bmatrix}.$$

The temporal and spatial evolution of concentration and structural order parameter fields are governed by the Cahn-Hilliard generalized diffusion equation and the time-dependent Ginzburg-Landau equation, respectively

$$\frac{\partial c_j}{\partial t} = \nabla\left(M(\phi)_j \nabla\left(\frac{\delta F}{\delta c_j}\right)\right) \tag{6}$$

$$\frac{\partial \phi_i}{\partial t} = -\sum_{k=1}^{\widetilde{N}} \frac{L_{ij}}{\widetilde{N}}\left(\frac{\delta F}{\delta \phi_i} - \frac{\delta F}{\delta \phi_k}\right) \tag{7}$$

where, $M(\phi)_j$ is the phase-dependent chemical mobility, $\widetilde{N}$ is the number of locally existing phases, and L_{ij} is a parameter that describes structural mobility. The phase-dependent mobility where the diffusivity in the ordered phases is assumed to be ¼ of in the matrix phase have shown to influence the kinetics of coprecipitate growth [10]. The phase dependent mobility is evaluated at each computational grid point using the expression $M(\phi) = M_{chem}\left(\phi_1 + \frac{1}{4}\sum_{i=2.5}\phi_i\right)$ The chemical mobility M_{chem} is calculated using the relationship $M_{chem} = \frac{\widetilde{D}}{V_m \frac{\partial^2 f'_c}{\partial (x^{\gamma'})^2}}$. A constant molar volume of $1*10^{-5}\ m^3 mol^{-1}$ is used for all phases. The inter-diffusivity ($\widetilde{D}$) between Nb and Ni is calculated using the prefactor ($D_0 = 8.8 \times 10^{-5}\ m^2 s^{-1}$) and activation energy ($Q = 272\ kJ\ mol^{-1}$) obtained from experimental studies of coarsening γ'' [20,21] in IN718. For numerical simplicity, we have used the same chemical mobility M_{chem} for both Al and Nb as coarsening studies [20,21] have reported fairly close values for activation energy for diffusion $\gamma'(Ni_3Al) - 298\ kJ/mol$ and $\gamma''(Ni_3Nb) - 272\ kJ/mol$. A value of $2.9 \times 10^{-11}\ m^2 N^{-1} s^{-1}$ was used for L_{ij} to guarantee diffusion-controlled growth. In our study, we also find that phase-dependent mobility also influences the characteristics of solute depletion zones around growing precipitates.

2.2. Properties of a critical nucleus

The properties of a γ'' critical nucleus (including its size and activation energy barrier) were calculated using the CNT [22,23]. The driving force for nucleation could be broken down as follows: $\Delta G = \Delta G_v - E^{self} - E^{int}$, where ΔG_v is the chemical driving force for nucleation, E^{self} is the self-elastic energy for forming a critical γ'' nucleus, and E^{int} is elastic interaction energy between an existing γ' precipitate and the γ'' nuclei. This study assumes that ΔG_v calculated from the thermodynamic database includes the contribution of E^{self} as both γ' and γ'' are coherent precipitates. The activation energy barrier ΔG^*_{hom} is calculated assuming a spherical geometry using the expression $\Delta G^*_{hom} = 16\pi\sigma^3/3\Delta G$. In CNT, the activation energy barrier for homogenous and heterogeneous nucleation can be correlated with each other as follows: $\Delta G^*_{het} = \theta(m,X) \times \Delta G^*_{hom}$, where $\theta(m,X)$ is a catalytic factor characterizing the potency of a heterogeneous nucleation site. In our case, $X = R_{\gamma'}/r_{\gamma''}$ and $m = (\sigma_{\gamma'\gamma} - \sigma_{\gamma''\gamma'})/\sigma_{\gamma''\gamma}$, where, $R_{\gamma'}$ is the radius of local curvature of γ', $r_{\gamma''}$ is the radius of a critical nucleus of γ'' (see Fig. 4(a)) and m is the cosine of the wetting angle formed by a γ'' embryo on the γ' surface. While calculating the catalytic factor, we consider a spherical cap of γ'' embryo forming from the γ matrix in contact with an existing γ' precipitate with a spherical shape of radius $R_{\gamma'}$ (Fig. 4(a)). Although the shape of the γ' particle is of a rounded cube rather than a sphere, the use of sphere-on-sphere nucleation is still justified as only a small area of the γ' surface influence the nucleation process. As will be shown later, a sphere could well approximate the geometry of the area that participates in the nucleation process. The analytical expression for the catalytic factor assuming sphere-on-sphere nucleation is as follows

$$\begin{aligned}\theta(m,X) \quad = \quad & \frac{1}{2} + \frac{1}{2}\left(\frac{(1-mX)}{u}\right)^3 + \frac{X^3}{2}\left[2 - 3\left(\frac{X-m}{u}\right)\right. \\ & \left. + \left(\frac{X-m}{u}\right)^3 + 3mX^2\left(\left(\frac{X-m}{u}\right) - 1\right)\right]\end{aligned} \tag{8}$$

where $u = (1 + X^2 - 2mX)^{\frac{1}{2}}$. The variations of $\theta(m,X)$ as a function of X at different values of m are presented in Fig. 4(b).

2.3. Statistical analysis

In phase field models, the nucleation procedure has to be explicitly incorporated as the governing equations like Cahn-Hilliard [24] and Allen-Cahn [25] do not allow for an increase in the system's free energy. This issue is usually overcome by adding the Langevin random force terms [26,27] into the governing equations to describe thermal fluctuation. But the Langevin force terms implemented in mesoscale phase field models are qualitative. They cannot be used for studying the coprecipitation problem as artificially large magnitudes of the random noise terms required to generate nuclei in reasonable computational time at mesoscale disrupt the existing parent microstructure. An alternative approach is the explicit nucleation algorithm (ENA) (see, e.g., Refs. [12–14]) in which nuclei of supercritical sizes are explicitly seeded stochastically (controlled by random number generators) into an existing microstructure following local nucleation rates given by the CNT:

$$J(r,t) = J_0(r,t)\exp\left(-\frac{\Delta G^*(\mathbf{r},t)}{k_B T}\right) \tag{9}$$

where $J(r,t)$ denotes local nucleation rates. The ENA offers flexibility in the choice of nucleation theories that can be used to calculate the activation energy barrier ΔG^* and pre-factor J_0. The calculations of ΔG^*_{hom} and ΔG^*_{het} are outlined in Section 2.2. In our case, the perfectors J_0^{hom} and J_0^{het} can be calculated by using the following equations

$$J_0^{hom} = N_0 Z\beta^* \tag{10}$$

$$J_0^{het} = N_{\gamma'} Z\beta^* \tag{11}$$

where Z is the Zeldovich factor and β^* represents the rate of attachment of atoms to the critical nucleus. The expressions for calculating Z and β^* can be found in [28]. N_0 is the nucleation site density for homogenous nucleation where all lattice sites are available; thus $N_0 = N_a/V$, where N_a is Avogadro's number, and V is the molar volume. In the case of heterogeneous nucleation on γ' precipitates, the number of available

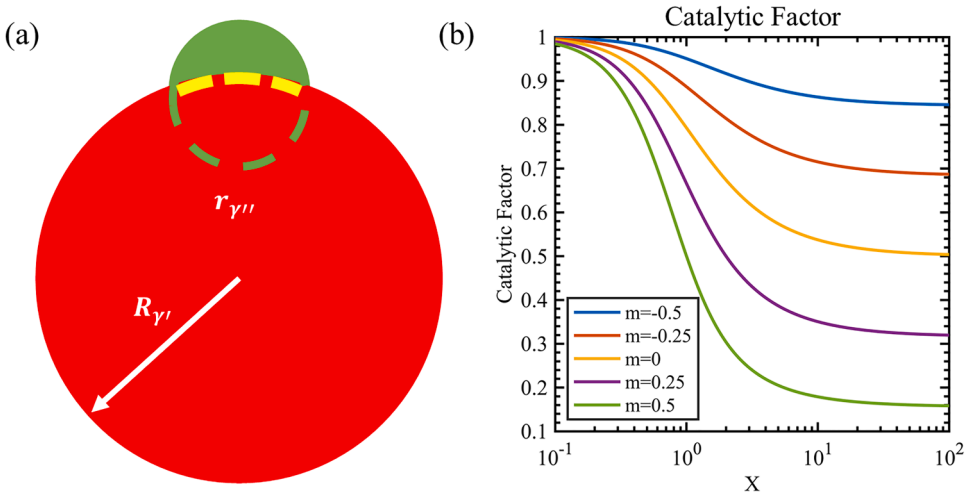

Fig. 4. (a) Schematic illustration of a γ'' phase nucleus at the surface of a spherical γ' precipitate. (b) Plot of catalytic factor for heterogenous nucleation as a function of X (local curvature of γ'/critical radius of γ'' nuclei) for different wetting angles (m).

sites decreases. To calculate $N_{\gamma'}$ as a function of γ' size, we use the following equation

$$N_{\gamma'} = n_{\gamma'} * A(\gamma')\delta\left(\frac{N_a}{v}\right) \tag{12}$$

where $n_{\gamma'}$ is the number of γ' particles per unit volume, A is the surface area of a γ' precipitate and δ is the interface thickness. The nucleation rate is then converted into probabilities as follows [12]

$$P(\mathbf{r},t) = 1 - \exp(-J(\mathbf{r},t)\Delta V \Delta t) \tag{13}$$

where P is the probability of forming a critical nucleus in a volume of ΔV during a time interval of Δt, predefined according to the length and time scale of the simulations. Nucleation events are then explicitly introduced into the microstructure by a probabilistic Poisson seeding process [12]. A uniformly distributed random number P_r between 0 to 1 is generated for every untransformed grid point in the computational cell for every time step Δt. A supercritical nucleus is implanted if $P(\mathbf{r},t) > P_r$. A solute depletion zone surrounding the implanted particle is created based on the Zener approximation [29] to ensure mass conservation.

Numerous phase field simulations using the explicit nucleation algorithm are required to sample different possible coprecipitate configurations based on the size of γ' and the time when γ'' nucleates. Since it is computationally expensive to run multiple 3D phase field simulations, we formulate a hybrid statistical analysis. ΔG^*_{het} of γ'' nucleation on the surface of γ' derived with the help of phase field simulations (to account for the elastic interactions) is used as input to analyze the nucleation events of γ''. The statistical analysis is then used to predict temporal periods within which heterogeneous nucleation of γ'' is most probable. The calculated ΔG^*_{het} is converted to nucleation rate using Eq. (9). The nucleation rate is subsequently converted to nucleation probabilities ($P(\mathbf{r},t)$) using Eq. (13). When the ENA is used for a single precipitate analysis, the resulting coprecipitate configurations are influenced by the sequence of the generated random numbers. To eliminate this bias, we ran 1,000 virtual experiments with the pre-calculated nucleation probabilities as a function of γ' size. Each run uses a unique series of random numbers to determine the time at which γ'' nucleates. Initially, when only γ' is present, the nucleation probability of γ'' will be the same on all six faces due to the cubic symmetry of γ'. In each virtual experiment, nucleation possibilities are checked by comparing the nucleation probability with a generated random number (different for each face) for discretized time increments corresponding to the time step in the phase field simulations. The event time is noted in the event of successful nucleation ($P(\mathbf{r},t) > P_r$). When the hybrid analysis is performed for subsequent nucleation of γ'', the nucleation probabilities can vary significantly for different faces based on the size of γ'. In such scenarios, the event time and the face at which successful nucleation happens are recorded.

2.4. Simulation setup

A spherical γ' precipitate of 2 nm is planted at the center of a 96 nm × 96nm × 96nm simulation box. Periodical boundary conditions are used along all three dimensions. The numerical grid size is chosen to be 0.5 nm so that the system is well resolved to study the evolution of the γ' particle from a small size. Two alloys with different Al/Nb ratios are considered to study the effect of alloy composition. Both compositions are chosen such that the γ' phase precipitates out first as we are interested in studying the formation of coprecipitates with the γ' phase being the core. The alloy compositions fall in the tie-triangle (Fig. 5) in the isotherm of the pseudo-ternary system. The two alloys analyzed in this study are referred to as Alloy A and Alloy B. Alloy A (Ni-4.8 at% Al-8.4 at % Nb) has a higher Al/Nb ratio than that of Alloy B (Ni-4.4 at%Al-8.6 at

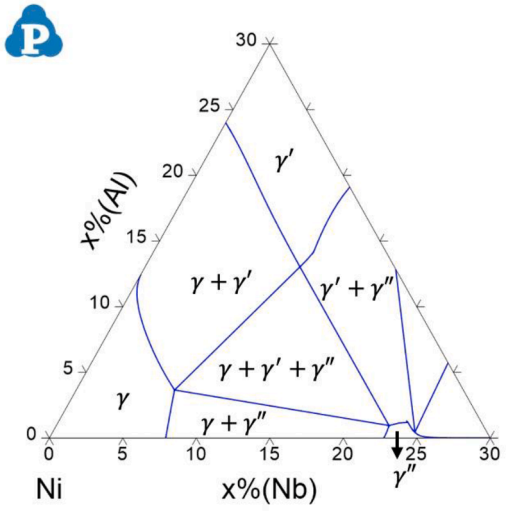

Fig. 5. Pseudo-ternary phase diagram at 720 C used in this study. Alloy compositions for multiphase coprecipitation simulations are chosen from the triangular region with three-phase equilibrium.

% Nb).

3. Simulation results

3.1. Activation energy barrier calculation

We compute ΔG^* for nucleation of γ'' in the following three different cases:

Case 1: Homogenous nucleation in the γ matrix far away from the γ' precipitate (not affected by the growth of the γ' precipitate)
Case 2: Homogenous nucleation in the γ matrix close to the γ' precipitate (affected by the growth of the γ' precipitate, i.e., within the solute depletion zone around the growing precipitate)
Case 3: Heterogenous nucleation at the coherent γ'/γ interface (i.e., with the consideration of the heterogeneous nucleation factor)

We have designed Cases 2 & 3 to highlight the individual effects of nucleation driving force and heterogeneous nucleation factor θ on ΔG^*. The cases are hereafter referred to as $\Delta G_i^* (i = 1,2,3)$. The equations used to calculate ΔG_i^* is outlined in Section 2.2. ΔG_1^* and ΔG_2^* increases with γ' precipitate size (Fig. 6(a)). This trend can be explained by the fact that the consumption of solute elements by the growth of γ', primarily Nb, decreases ΔG_v (the absolute value). Also $\Delta G_1^* < \Delta G_2^*$ because locations in the matrix away from the γ' precipitate is less affected by the solute depletion zone formed around the growing precipitate. To calculate ΔG_3^*, $\theta(m, X)$ must be calculated as a function of γ' size. We assume sphere-on-sphere nucleation (Fig. 4(a)) to calculate the heterogenous nucleation factor because it is the local curvature of the γ/γ' interface rather than the overall shape of the γ' precipitate that impacts the activation energy barrier. When γ' is small, it assumes a shape close to a sphere to minimize the interfacial energy. However, as γ' becomes larger, the elastic energy dominates over the interfacial energy, making it cuboidal. The changes in shape are presented in Fig. 7(a, b). As

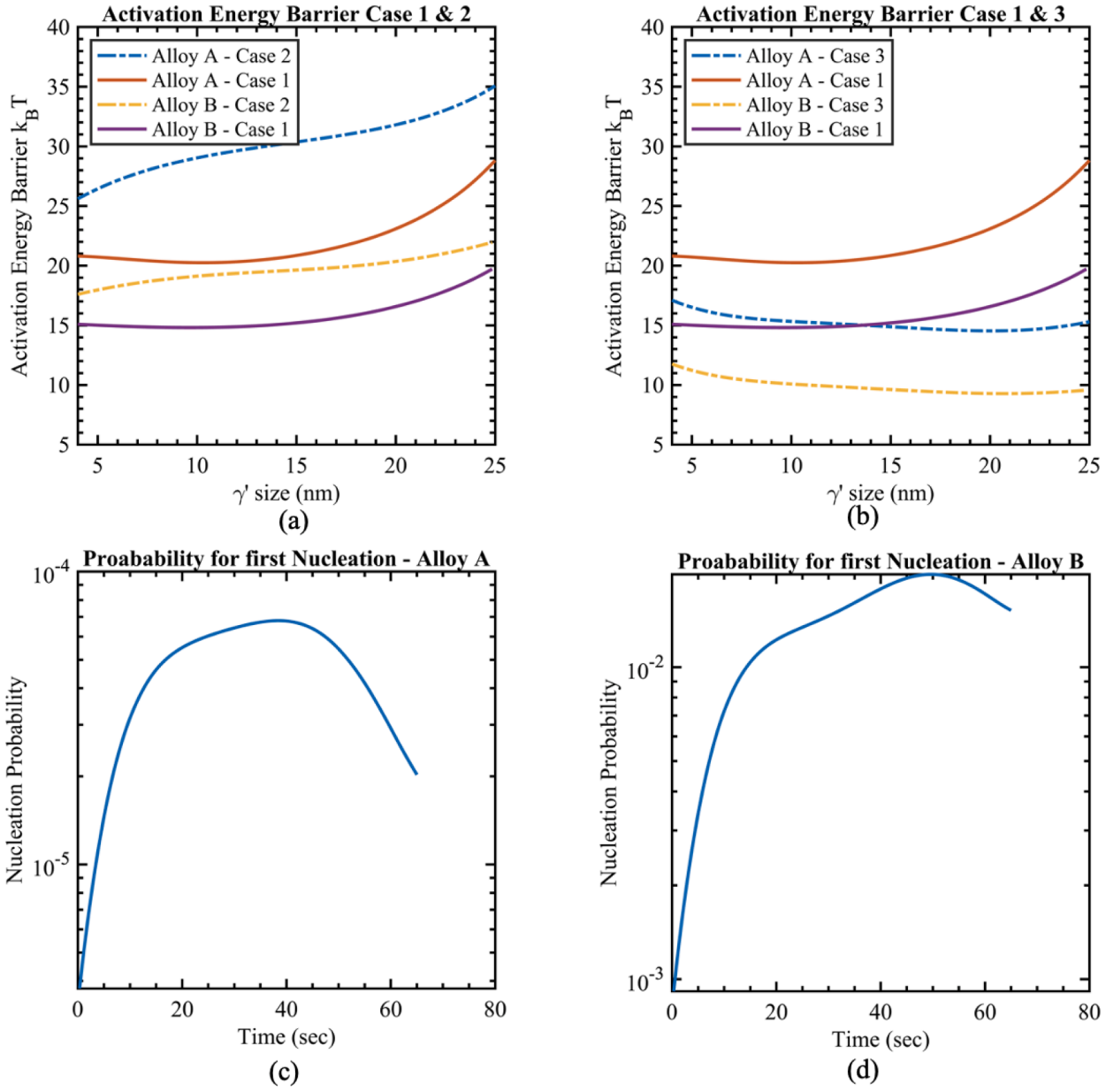

Fig. 6. Activation energy barrier for (a) homogenous nucleation and (b) heterogeneous nucleation of Alloy A and B, respectively. (c) & (d) Conversion of the activation energy barrier to nucleation probability for Alloy A and B.

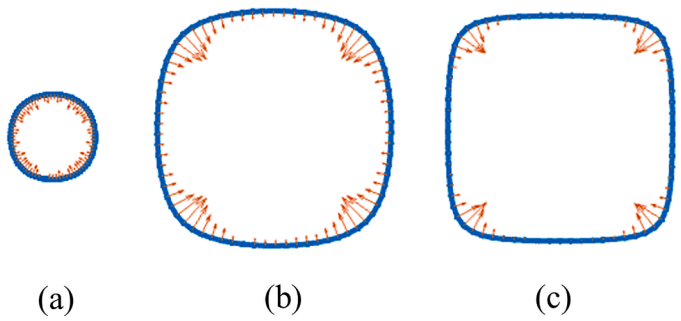

Fig. 7. 2D cross-section of γ' at (a) 4nm, (b) 14nm, and (c) 12 nm with twice of the lattice misfit. The magnitude of the red arrows represents the local curvature of γ' surface in the (001) plane.

mentioned in Section 2.2, two parameters, X (ratio between the local radius of curvature of the γ/γ' interface where nucleation occurs and the radius of the γ'' critical nuclei) and m (the wetting angle), are inputs to Eq. (8) in calculating the heterogenous nucleation factor. The local radius of curvature used for the calculation of parameter X is presented in Fig. 8(b). To calculate the wetting angle, we estimate the average interfacial energy (Fig. 8(c)) of the γ'/γ'' interface (dashed yellow-red line segment in Fig. 4(a)) along {100} faces for the 3 variants of γ''. Finally, the heterogeneous factor calculated using parameters X and m is presented in Fig. 8(d). $\Delta G_3^* = \theta(m, X) \times \Delta G_2^*$ is compared with ΔG_1^* in Fig. 6(b). Once the heterogeneous factor is multiplied with ΔG_2^*, we see that for the chosen alloy compositions, heterogeneous nucleation of γ'' at the γ'/γ interface is always preferred over homogenous nucleation from the γ matrix.

3.2. Statistical analysis

3.2.1. The first nucleation event of γ''

In this section, we present our results from the hybrid statistical approach presented in Section 2.3. Since we have shown that heterogeneous nucleation at the γ'/γ interface is always preferred over homogenous nucleation we provide ΔG_3^* of Alloy A and B as input to the hybrid explicit nucleation routine. The nucleation rates of γ'' for Alloy A and Alloy B are calculated using Eq. (9). They are further converted to

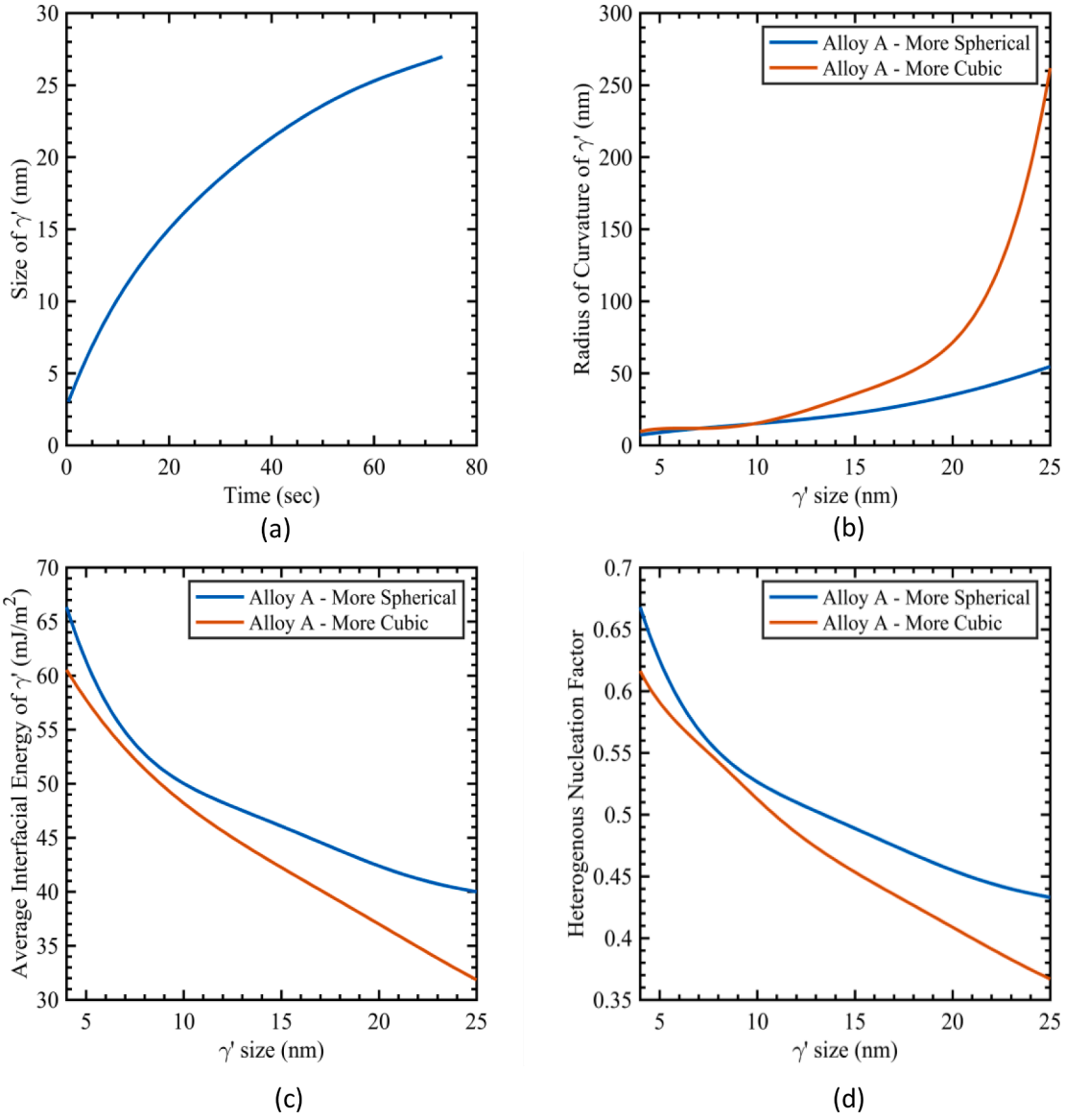

Fig. 8. Plots showcasing (a) γ' size as a function of time, (b) maximum curvature as a function of γ', (c) average interfacial energy of the γ'/γ'' interface as a function of time and (d) heterogeneous factor as a function of time for Alloy A with two different misfits.

nucleation probabilities using Eq. (13). To ensure that the stochastic nature of nucleation is preserved in this analysis, 1,000 virtual experiments are conducted to determine the time for the first nucleation event in Alloys A and B by using the algorithm discussed in Section 2.3. The time for the first nucleation event of γ'' is presented in Fig. 9(a), where the x-axis represents the simulation time intervals for the first nucleation event, and the y-axis represents the number of experiments where the first nucleation event occurred between a specific time interval. The size of γ' at the time intervals could be correlated with the γ' size using the plot presented in Fig. 8(a). In the case of Alloy A, most nucleation events occur between 15 and 30 s, where the size of γ' is around 12 to 16 nm. This time interval corresponds to the hump in the nucleation probability (Fig. 6(c, d)). The higher Al/Nb ratio can explain the delayed nucleation, which leads to a lower chemical driving force. However, as γ' grows, the development of a flatter interface significantly reduces the activation energy barrier. In the case of Alloy B, most nucleation events occur between 0 and 5 s (Fig. 9(b)), when the size of γ' is below 5 nm. The lower Al/Nb ratio provides enough driving force despite the smaller contribution from the heterogeneous factor in reducing ΔG^*_{het}.

3.2.2. Subsequent nucleation events of γ''

To study the effect of the first nucleation event on subsequent ones, one of the {100} faces is seeded with a γ'' nucleus. Then the system is allowed to evolve and ΔG^* is tracked on the opposite and adjacent faces of the γ' particle. Because of the four-fold symmetry of the γ' shape, it is sufficient to account for one of the four adjacent faces. For Alloy A, the first nucleation event occurs when the γ' particle is around 14 nm in size. In the case of Alloy B, the first nucleation event occurs when the γ' particle is around 4 nm in size. ΔG^*_{het} for the second nucleation event of γ'' in Alloy A and B are presented in Fig. 10(a) and (b), respectively. The Nb solute depletion zone formed due to the presence of the first γ'' particle is presented in Fig 10(c) and (d) for Alloy A and Alloy B, respectively. In the case of Alloy A, the difference between ΔG^*_{het} for the adjacent and opposite faces is not significant.

4. Discussion

In previous studies [7,8], the formation of coprecipitate configurations was primarily attributed to alloy chemistry and lattice compatibility between the γ' and γ''. While these factors do play important roles, we have found that it is the interplay among many different factors that determines the final coprecipitate configurations ranging from highly symmetric sandwich coprecipitates to a large γ' fully (compact) or partially coated with γ'' precipitates.

4.1. Influences of alloy composition and driving force for nucleation

The experimental studies by both Cozar and Pineau [7] and Detor et al. [9] have shown that varying the (Ti+Al/Nb) ratio while keeping concentrations of the other elements constant results in vastly different coprecipitate microstructures. To analyze the effect of alloy composition, we performed high throughput calculations using Pandat Software with the PanNi2020 database from CompuTherm. The driving forces for nucleation of γ' and γ'' in a range of alloy compositions were calculated. The driving force for γ' nucleation increases with increasing Al and Nb concentrations. In contrast, the driving force for γ'' nucleation increases with increasing Nb concentration but decreases with increasing Al concentration (see Fig. 3). A line scan of the Al and Nb concentration field along the γ' precipitate in the [100] direction is presented in Fig. 11 (b). The Al and Nb depletions at the γ/γ' interface are apparent. Thus, from purely a chemical driving force point of view, locations in the γ matrix far away from the precipitate are more preferred sites for the nucleation of γ''.

4.2. Influence of elastic interaction energy due to the presence of γ'

To assess the contribution from elastic interaction between the pre-existing γ' precipitate and a nucleating γ'' particle, the equilibrium shape of a γ' precipitate was first obtained. The variations of E_{int} for nucleation of variant 1 of γ'' around the γ' is presented in Fig. 11(a). From the definition of driving force for nucleation presented in Section 2.2, it can be concluded that a negative value of E_{int} would increase ΔG which in turn decreases ΔG^* for nucleation. It can be seen from the contour plot that the most negative values of E_{int} occur near the faces of γ' that are parallel to the (100) planes, which happen to be the habit plane of variant 1 of γ''. Similarly, E_{int} of variant 2 and 3 of γ'' would be most negative on faces of γ' that are parallel to (010) and (001) planes, respectively. Thus, the contribution from E_{int} favors heterogeneous

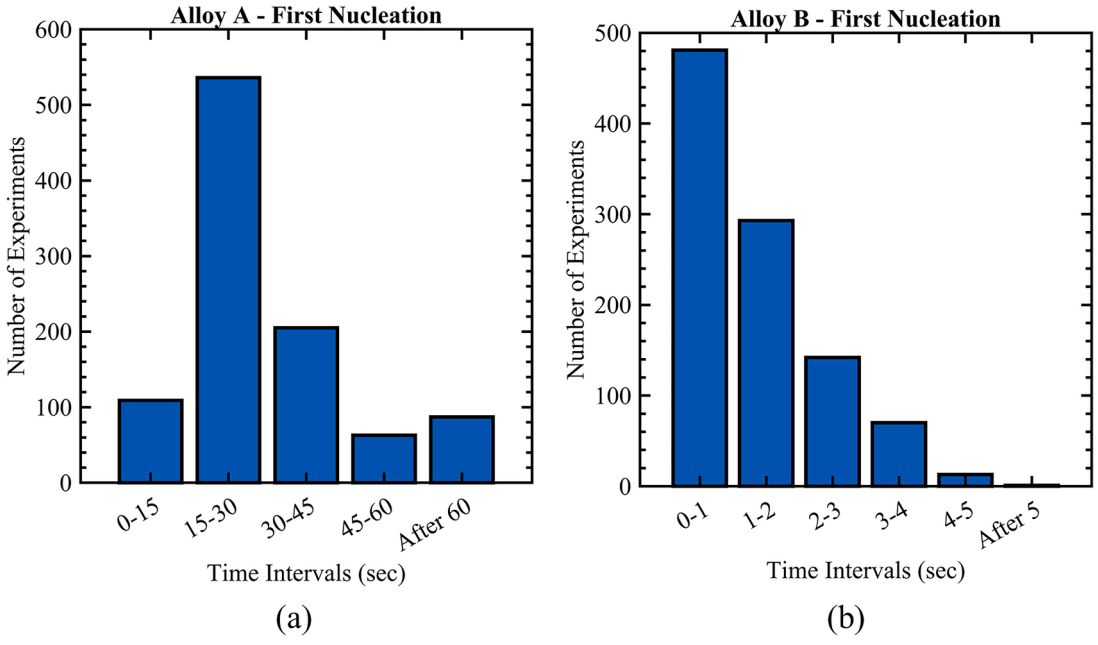

Fig. 9. Bar plots records nucleation events of the first γ'' nuclei for different time intervals for (a) Alloy A and (b) Alloy B.

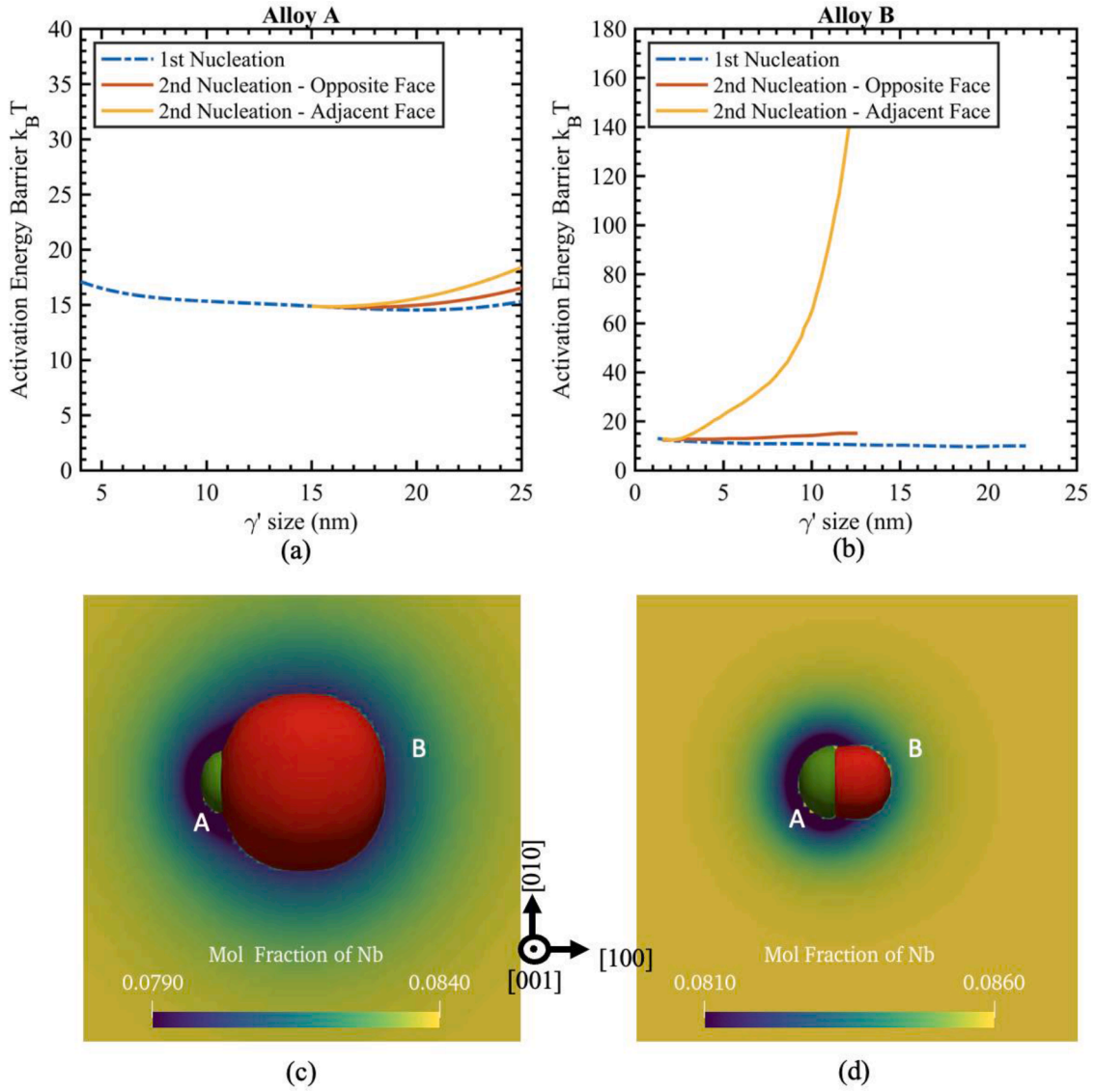

Fig. 10. Line plots for the activation energy barrier for subsequent nucleation of γ'' for (a) Alloy A and (b) Alloy B. 2D sliced plots of the (001) plane of the simulation box showing the Nb concentration for (c) Alloy A and (d) B. The bright red region in the middle of the simulation box is the γ' precipitate, whereas the green contour represents γ'' precipitate. The dark blue region (A) is the solute depletion zone associated with the γ''

nucleation of γ'' on γ' faces over homogenous nucleation in the matrix. Although, E_{int} decreases ΔG^*, the magnitude of E_{int} is two orders of magnitude smaller than that of the chemical driving force. The difference in the overall elastic energy between a coprecipitate configuration and the monolithic counterpart has been reported by Phillips, P. J., et al. [30] also shows that the coprecipitate morphology has a lower elastic energy. Such coprecipitate configurations were also observed in Al alloys [31]. The significance of having misfits of different signs for two interacting precipitate phases has also been explored by Bhadak et al. [32]. Their study has shown that when a cubic and a tetragonal phase have opposite signs of misfit, they have negative elastic interaction energy and prefer a coprecipitate configuration so that the overall elastic energy is reduced. However, if the misfits of the precipitate phases are the same either a dilatational tension or compression field is created around the precipitatesare elastically repulsive and would prefer to stay as monoliths.

4.3. Influence of solute depletion zone

The simulation results of the Nb concentration field around the growing γ' and γ'' particles are shown in Fig. 10(c, d). The depletion zone associated just with the growing γ' precipitate has been characterized by a greenish blue hue (marked as B in Fig. 10(c, d)). The nucleation of γ'' consumes more Nb from the γ matrix, and the depletion zone associated with it has been characterized with the dark blue zone (marked as A in Fig. 10(c, d). The Nb depletion zone associated with γ'' formation is more extensive around the smaller γ' precipitate (Alloy B, Fig. 10(d)) as compared to that around the larger γ' precipitate (Alloy A, Fig. 10(c)), covering partially the adjacent (010) and (001) faces of the γ' particle,

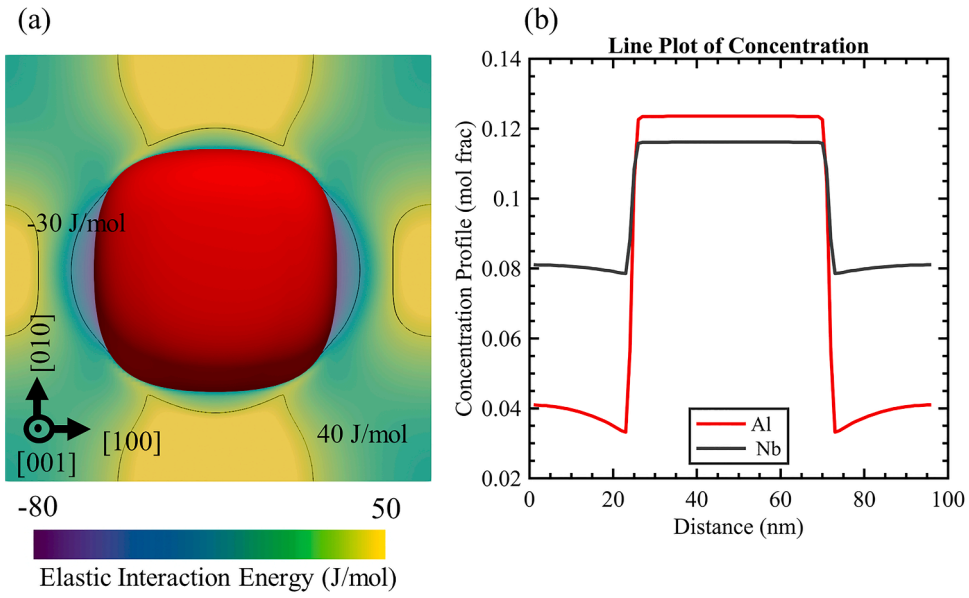

Fig. 11. (a) Elastic interaction energy field arising from interactions between a growing γ' precipitate (red contour) and a nucleating γ'' particle; (b) concentration profile across the center of the γ' precipitate along the [100] direction.

making γ'' nucleation on those faces highly unlikely. The opposite (100) face is the only face that could harbor another γ'' nucleus and, hence, lead to a sandwich coprecipitate. When the size of the γ' particle becomes > 10 nm, the Nb depletion zone does not affect the nucleation of γ'' on adjacent faces (i.e., (010) and (001) faces) significantly. Thus, the concentration fields favor the formation of a compact coprecipitate. These simulation results seem to be consistent with the observation made by Cozar and Pineau [7] that there is a critical γ' size that is required to form the compact coprecipitates.

Additionally, we have performed a simulation with the same chemical mobility across all 3 phases to investigate the effect of phase-dependent mobility. In this case, the growing γ'' can deplete Nb even in the vicinity of the opposite face of γ' (Fig. 12(b)). In the case of reduced mobility in the ordered phases (γ' and γ''), the flux of Nb that passes through the γ' core is reduced. Thus, the depletion zone on the opposite face is not as pronounced (Fig. 12(a)). Shi et al. [10] have discussed the implications of having reduced mobility in the later growth stage of the coprecipitates. With the reduced mobility assumption, it was found that γ'' acted as a better diffusional barrier for Al transport from the γ matrix to the γ' core.

4.4. *Influence of interfacial energy anisotropy and γ' shape*

One of the characteristic features of both the sandwich and compact coprecipitate configurations is the nearly flat interface between γ' and γ''. The influence of this highly anisotropic interfacial energy on the formation of coprecipitates is twofold. Firstly, ΔG^*_{het} is significantly reduced when the γ'/γ interface becomes more aligned with the {100} atomic planes as γ' grows into a cuboidal shape from being spherical initially. Although the homogeneous component (ΔG^*_2 – Case 2) of ΔG^*_{het} increases with an increase in γ' size, ΔG^*_3 - Case 3 ($\Delta G^*_3 = \theta(m, X) \times \Delta G^*_2$) is reduced due to a decrease in the average γ'/γ''

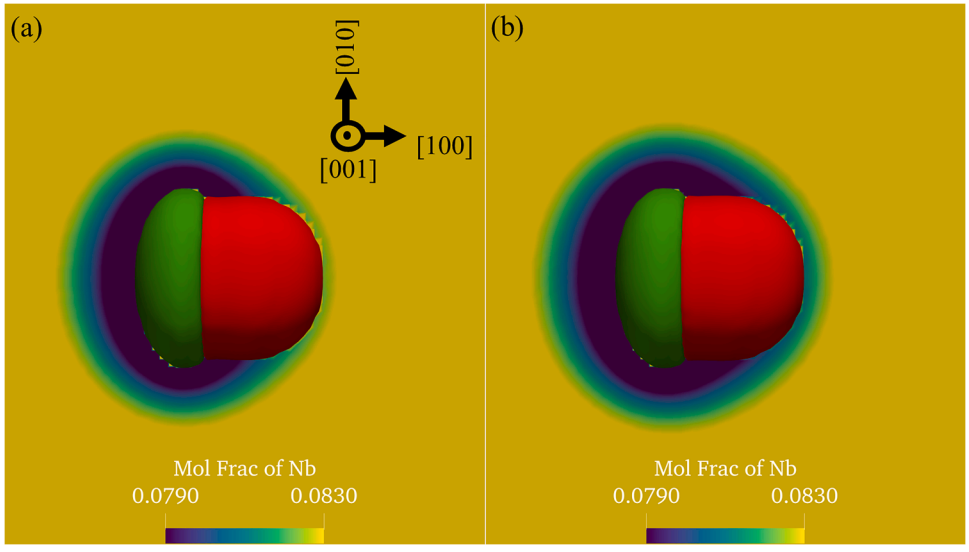

Fig. 12. 2D sliced plot of Nb concentration for (a) simulation with reduced diffusivity among the ordered phases and (b) simulation with the same diffusivity among the ordered and matrix phase.

interfacial energy (average over the inclinations of the yellow dash line in Fig. 4(a)). Secondly, the shape of the γ' particle influences the effect of interfacial energy anisotropy on the reduction of ΔG^*_{het}. To study the influence of γ' shape, a parametric study was performed by altering the precipitate shape by increasing the elastic energy over the interfacial energy ratio of γ' by a factor of 2. This resulted in flatter faces (Fig. 7(c)). Fig. 8(b, c) presents the average interfacial energy and maximum curvature. It is readily seen that the presence of flatter faces at γ/γ' interface reduces the heterogenous nucleation factor significantly (Fig. 8(d)), enabling γ'' to nucleate at all faces at a smaller γ' size leading to the formation of compact morphology.

4.5. Evolution of sandwich and compact coprecipitate morphologies

The formation of coprecipitates in Alloy A and B are simulated using the explicit nucleation algorithm [12] in the phase field model, where we used ΔG^*_{het} calculated on neighboring and opposite faces (Fig. 10(a, b)) to seed γ'' nuclei in an existing microstructure. In the case of Alloy A, the first γ'' precipitate nucleates when γ' is 14 nm (Fig. 13(a)). The subsequent nucleation of γ'' occurs on neighboring and opposite faces (Fig. 13(b, c)). All six faces are coated with γ'' when γ' is around 20 nm in size (Fig. 13(c)). From statistical analysis of the nucleation events, we can conclude that the probability of forming a fully coated or partially coated compact coprecipitate is more than 80% in Alloy A.

In the case of Alloy B, the first nucleation event of γ'' occurs before γ' grows to a size of 5 nm (Fig. 14(a)). Such early nucleation of γ'' eliminates the possibility of forming compact coprecipitates. A time gap of 1 s and 3 s between nucleation of the second γ'' on the opposite face results in either a nearly symmetric (Fig. 14(d, e)) or an asymmetric (Fig. 14(b, c)) sandwich coprecipitate. We see a mixture of symmetric and asymmetric sandwich coprecipitates from the experimental observations presented in Fig. 1(b, d).

4.6. Coprecipitate morphologies with γ'' core

Detor et al. [9] observed that for alloys with a lower (Al+Ti)/Nb ratio, the core of the coprecipitates changed from γ' to γ''. To analyze this phenomenon, we choose to simulate the formation of a coprecipitate in Alloy C (3.6 at% Al and 8.1 at% Nb), whose Al/Nb ratio is lower than Alloy A and B. Since the activation energy barrier for homogenous nucleation of γ'' is smaller than that for γ' in Alloy C, on isothermal aging at 720 °C, γ'' would precipitate out first. The ΔG^*_{het} for nucleation of γ' at γ''/γ interface and ΔG^*_{hom} for homogenous nucleation of γ' in the γ matrix are presented in Fig. 15(a). The methodology described in Section 2.2 was used to calculate ΔG^*. In the case of a growing γ' precipitate, a solute depletion zone of both Al and Nb is developed in its vicinity. However, in the case of a growing γ'' precipitate, an Al enrichment zone (Fig. 15(c)) and an Nb depletion zone (Fig. 15(b)) are developed. As both Al and Nb are γ' stabilizers, the chemical driving force for the nucleation of γ' at the vicinity of γ'' is determined by the relative enrichment and depletion of Al and Nb, respectively. In terms of the γ'/γ'' interfacial energy anisotropy and the elastic interaction energy both favor the nucleation of γ' on the broad face of the disk-shaped γ'' particle (Fig. 15(d, e)). As γ'' grows, the broad face becomes more favorably oriented along [100], resulting in a larger value of m (the cosine of the wetting angle), which results in a significantly smaller catalytic factor (refer to Fig. 4(b)). As shown in Fig. 15 (a), these factors enable γ' to nucleate homogeneously in the matrix when γ'' is below 12 nm in size ($\Delta G^*_{hom} < \Delta G^*_{het}$). However, when γ'' grows larger, heterogeneous nucleation of γ' at γ''/γ interface becomes preferred ($\Delta G^*_{hom} > \Delta G^*_{het}$).

4.7. Microstructure map of coprecipitate morphologies

Based on the above simulation results, a microstructure map that shows possible coprecipitate morphologies in Al-Nb composition space is presented in Fig. 16. To plot the microstructure map, we start by calculating the nucleation rates for homogenous precipitation of both γ' and γ'' using Eq. (9). The calculated nucleation rates for γ' and γ'' are normalized by their sum for a specific composition. The microstructure map is first divided into four sections representing regions where the first nucleating precipitate is γ' (red), γ'' (green), simultaneous nucleation of γ' and γ'' (red+green) and a region of negligible nucleation. The three alloy compositions considered in this study are plotted, and the estimated boundaries for the several coprecipitate morphologies explored in this study are drawn on the microstructure map. Statistical analysis of other alloy compositions should result in a more accurate microstructure map that will be useful in alloy design.

5. Limitations of the model

This study uses a pseudo-ternary system to represent the 7-component system of Inconel 718. Generally, when reducing a multicomponent system to a pseudo-ternary system, the γ' phase stabilizers will be mapped onto Al, while the γ'' stabilizers will be mapped onto Nb. The Inconel 718 system poses a unique challenge as elements such as Ti and Nb are present in both γ' and γ'' phases, and different elements may

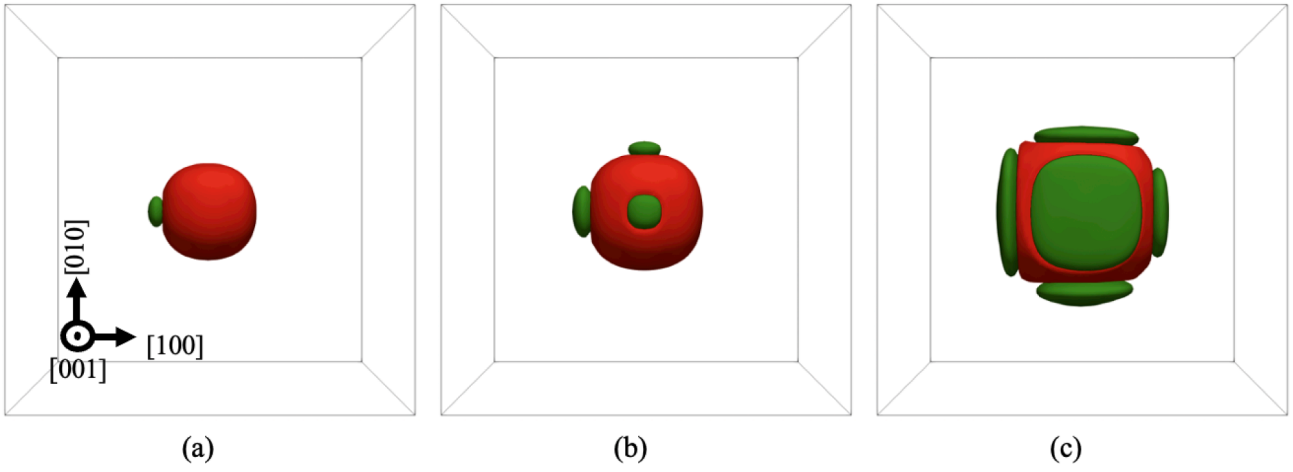

Fig. 13. Evolution of compact coprecipitate showcasing (a) first γ'' nuclei when γ' is 14 nm, (b) two other variants of γ'' that had been nucleated with a time gap of 6 sec, and (c) the evolved compact coprecipitate with all faces coated with γ''

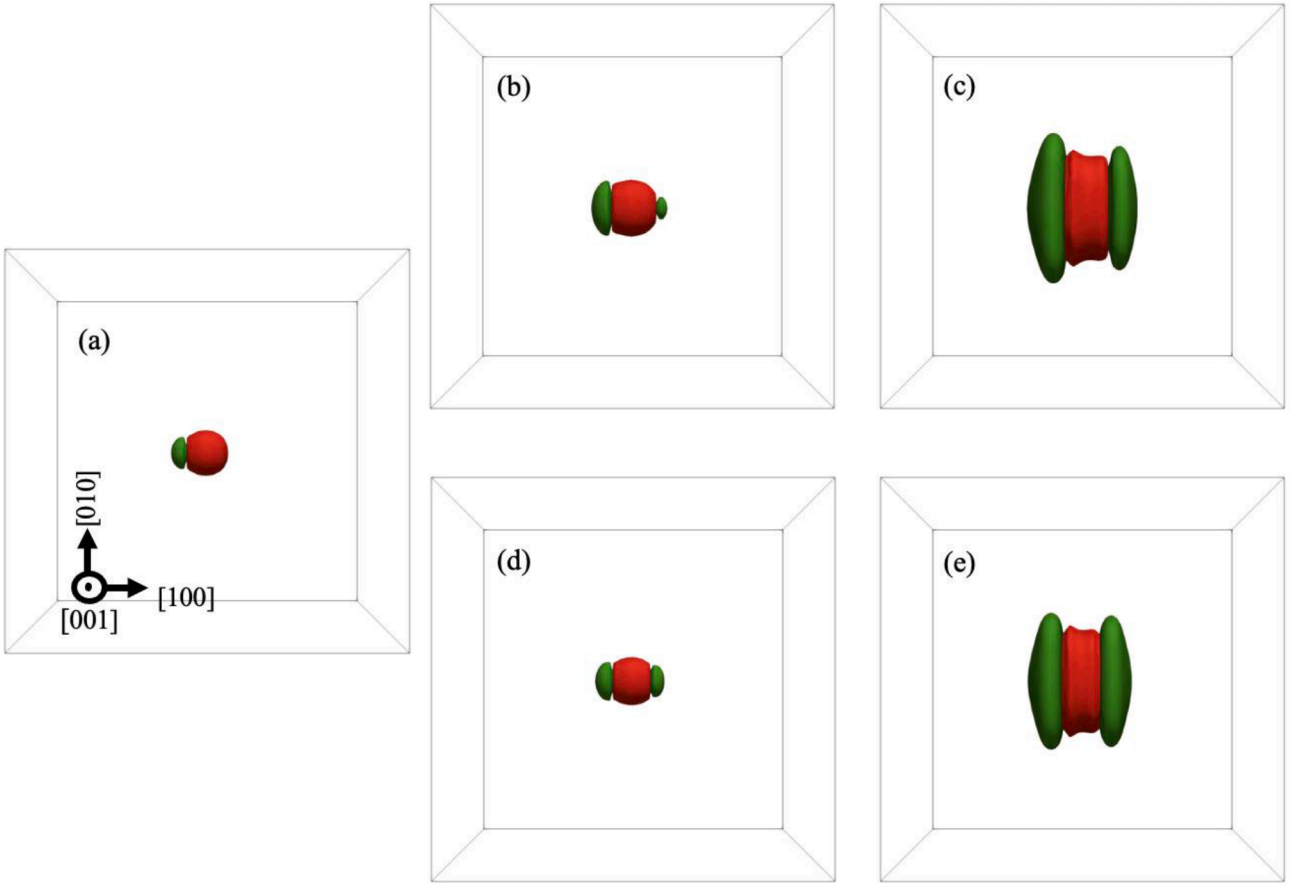

Fig. 14. Microstructure evolution to form symmetric and asymmetric sandwich coprecipitate showcasing (a) first nucleation of γ'' when γ' is 4nm, (b) the second γ'' nucleates with a 3-sec delay on the opposite face, (c) the evolved asymmetric sandwich coprecipitate, (d) the second γ'' nucleates with a 1-sec delay on the opposite face and (e) the evolved symmetric sandwich coprecipitate

have different atomic mobilities that will affect the composition within the depletion zone. The chemical driving force for nucleation estimated through the approximated database, though similar in magnitude, may not be accurate, as shown in Fig. 3. However, the analysis could be extended to incorporate more accurate chemical driving force and atomic mobility data straightforwardly. The interfacial energies used in this study are qualitative as they are difficult to determine from experiments. However, we have ensured in the formulation of our model that it can capture the flat γ'/γ'' interface. Additionally, a comparison of the equilibrium triple junction angles between experiment observation and simulation prediction could also help in the determination of ratio of interfacial energies between the different phases. Although, its straightforward to obtain this quantity from the phase field simulations [17], extracting the angle from the experiment images poses significant challenges. Firstly, it is difficult to resolve the γ'/γ interface due to the lack of distinguishing features using STEM- HAADF imaging (as shown in Figs. 1 and 2). Although the use of EDS mapping results in well-defined interfaces, we are limited by the resolution of the technique to accurately measure the triple junction angle.

6. Summary

We have investigated factors that influence the formation of compact and sandwich coprecipitate microstructures using a combination of phase field simulations and statistical analysis based on an explicit nucleation algorithm derived from the classical nucleation theory. We began our analysis by calculating the activation energy barrier, ΔG^*, for homogenous and heterogeneous nucleation of γ'' in the presence of γ'. The calculated ΔG^* was used as an input to study the subsequent nucleation of γ'' on γ'. Previous studies [7,8] have tried to explain the formation of coprecipitates primarily through the lens of the ratio of solute elements such as Al, Nb, and Ti. Also, the studies hypothesized that the solute depletion zone formed due to the nucleation of γ'' on one of the faces of γ' plays a crucial role in determining the final coprecipitate configuration. Through our detailed analysis using phase field simulation and statistical analysis, we have concluded that the interplay among these and many other factors determine what coprecipitate configurations form, as summarized below.

1 The role played by the alloy composition in the formation of different coprecipitate configurations could be understood in terms of the ratio of γ' stabilizers (Al and Nb) to that of γ'' stabilizers (Nb). To obtain a coprecipitate configuration with γ' core (sandwich or compact), the alloy composition must have a higher Al/Nb ratio. Such a ratio favors nucleation of γ' first and induces a delay in γ'' nucleation. However, a lower Al/Nb ratio would lead to the formation of coprecipitates with γ'' as the core. Finally, a very high Al/Nb ratio would lead to a microstructure with a high volume fraction of γ' at the cost of γ'' and there will not be enough γ'' to form compact coprecipitates with sufficient γ'' coating. The findings are visualized in the microstructure map.
2 By calculating the catalytic factor and the activation energy barrier as a function of γ' size, we show that there exists a critical γ' size for the formation of compact coprecipitates. The critical γ' size is dependent on γ'/γ'' interfacial energy, the shape of the γ' core and the size of the depletion zone associated with the growing γ''. Although the driving force for γ'' nucleation decreases as γ' becomes larger, the

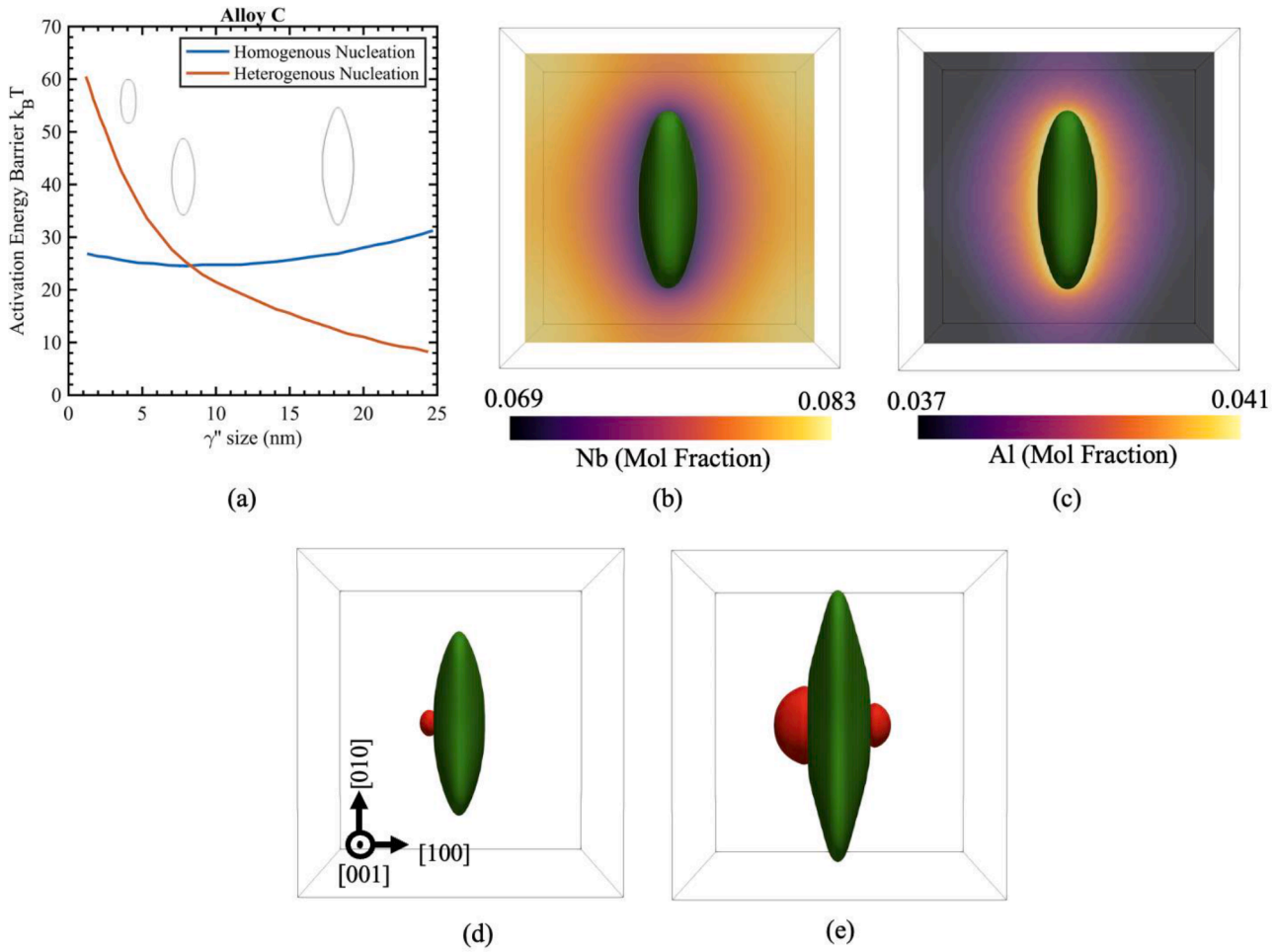

Fig. 15. (a) A line plot of the ΔG^* for both homogeneous and heterogeneous nucleation of γ' for Alloy C: the γ'' shapes at different sizes are embedded in a 2D sliced plot of (b) Nb and (c) Al concentration fields(the green contour represents γ''precipitate, whereas the blue and yellow region, represents the Nb depletion zone and Al enrichment zone) (d) and (e) shows the evolution of a coprecipitate with γ''as the core.

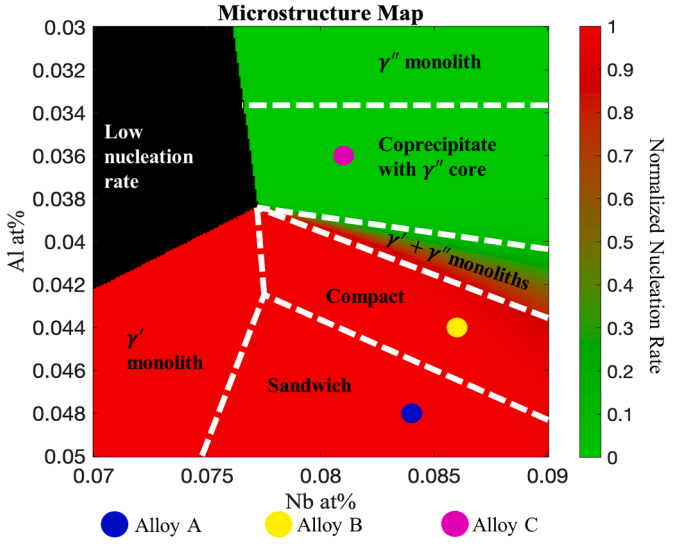

Fig. 16. Microstructure map for formation of different coprecipitate morphologies shown in Al and Nb compositional space. The color bar indicates the normalized homogenous nucleation rate - $J^{\gamma'}/(J^{\gamma'}+J^{\gamma''})$

change from spherical to the cuboidal shape of the γ' core aids in reducing the catalytic factor. Additionally, when γ' is larger than the critical size, the solute depletion zone associated with a nucleated γ'' has limited influence on γ'' nucleation on the adjacent faces.

3 Through a parametric study of the shape evolution of γ', we can conclude that by increasing the lattice misfit between γ and γ', the critical size required to form compact coprecipitates could be reduced. This will lead to a microstructure with finer compact coprecipitates.

4 The total driving force for nucleation is primarily dominated by the chemical driving force, which is two orders of magnitude higher than the elastic interaction energy.

Although the above-listed conclusions are derived based on analyses of isothermal ageing, they are also applicable to non-isothermal heat treatments. The heterogeneous nucleation factor (shape dependent) calculated in this study could be used with driving force data of non-isothermal processes to determine the critical cooling rate at which γ' attains the critical size before γ'' nucleation starts. Such a heat treatment would lead to primarily compact coprecipitates.

Declaration of Competing Interest

The authors declare that they have no known competing financial interests or personal relationships that could have appeared to influence the work reported in this paper.

Acknowledgment

We acknowledge the financial support from the NSF DMREF program under grant DMR-1922239. We also thank Dr. Fan Zhang from CompuTherm for providing the thermodynamic databases used in this study.

References

[1] L. Capuano, International energy outlook 2018, U.S. Energy Information Administration, n.d. https://www.eia.gov/outlooks/ieo/executive_summary.php.
[2] M. Sundararaman, P. Mukhopadhyay, S. Banerjee, Precipitation of the δ-Ni3Nb phase in two nickel base superalloys, MTA 19 (1988) 453–465, https://doi.org/10.1007/BF02649259.
[3] R.C. Reed, The Superalloys: Fundamentals and Applications, 1st ed., Cambridge University Press, 2006 https://doi.org/10.1017/CBO9780511541285.
[4] A.R.P. Singh, S. Nag, J.Y. Hwang, G.B. Viswanathan, J. Tiley, R. Srinivasan, H. L. Fraser, R. Banerjee, Influence of cooling rate on the development of multiple generations of γ′ precipitates in a commercial nickel base superalloy, Mater. Charact. 62 (2011) 878–886, https://doi.org/10.1016/j.matchar.2011.06.002.
[5] D. Paulonis, J. Oblak, D. Duvall, Precipitation in Nickel-base Alloy 718, Pratt and Whitney Aircraft, Middletown, Conn, 1969.
[6] J.M. Oblak, D.F. Paulonis, D.S. Duvall, Coherency strengthening in Ni base alloys hardened by DO22 γ′ precipitates, Metall. Mater. Trans. B 5 (1974) 143, https://doi.org/10.1007/BF02642938.
[7] R. Cozar, A. Pineau, Morphology of γ' and γ" precipitates and thermal stability of inconel 718 type alloys, Metall. Trans. 4 (1973) 47–59, https://doi.org/10.1007/BF02649604.
[8] J. He, G. Han, S. Fukuyama, K. Yokogawa, Interfaces in a modified Inconel 718 with compact precipitates, Acta Mater. 46 (1998) 215–223, https://doi.org/10.1016/S1359-6454(97)00221-8.
[9] A.J. Detor, R. DiDomizio, R. Sharghi-Moshtaghin, N. Zhou, R. Shi, Y. Wang, D. P. McAllister, M.J. Mills, Enabling large superalloy parts using compact coprecipitation of γ′ and γ′′, Metall. Mater. Trans. A 49 (2018) 708–717, https://doi.org/10.1007/s11661-017-4356-7.
[10] R. Shi, D.P. McAllister, N. Zhou, A.J. Detor, R. DiDomizio, M.J. Mills, Y. Wang, Growth behavior of γ ' /γ ' ' coprecipitates in Ni-Base superalloys, Acta Mater. 164 (2019) 220–236, https://doi.org/10.1016/j.actamat.2018.10.028.
[11] J. Coakley, D. Dye, H. Basoalto, Creep and creep modelling of a multimodal nickel-base superalloy, Acta Mater. 59 (2011) 854–863, https://doi.org/10.1016/j.actamat.2010.08.035.
[12] J.P. Simmons, C. Shen, Y. Wang, Phase field modeling of simultaneous nucleation and growth by explicitly incorporating nucleation events, Scr. Mater. 43 (2000) 935–942, https://doi.org/10.1016/S1359-6462(00)00517-0.
[13] Y.H. Wen, J.P. Simmons, C. Shen, C. Woodward, Y. Wang, Phase-field modeling of bimodal particle size distributions during continuous cooling, Acta Mater. 51 (2003) 1123–1132, https://doi.org/10.1016/S1359-6454(02)00516-5.
[14] Y.H. Wen, B. Wang, J.P. Simmons, Y. Wang, A phase-field model for heat treatment applications in Ni-based alloys, Acta Mater. 54 (2006) 2087–2099, https://doi.org/10.1016/j.actamat.2006.01.001.
[15] I. Steinbach, F. Pezzolla, A generalized field method for multiphase transformations using interface fields, Phys. D 134 (1999) 385–393, https://doi.org/10.1016/S0167-2789(99)00129-3.
[16] I. Steinbach, Phase-field models in materials science, Model. Simul. Mater. Sci. Eng. 17 (2009), 073001, https://doi.org/10.1088/0965-0393/17/7/073001.
[17] W. Guo, R. Spatschek, I. Steinbach, An analytical study of the static state of multi-junctions in a multi-phase field model, Phys. D 240 (2011) 382–388, https://doi.org/10.1016/j.physd.2010.09.014.
[18] N. Ma, Q. Chen, Y. Wang, Implementation of high interfacial energy anisotropy in phase field simulations, Scr. Mater. 54 (2006) 1919–1924, https://doi.org/10.1016/j.scriptamat.2006.02.005.
[19] A.G. Khachaturian, Theory of structural transformations in solids, 1983. https://www.osti.gov/biblio/5821133.
[20] A. Devaux, L. Nazé, R. Molins, A. Pineau, A. Organista, J.Y. Guédou, J.F. Uginet, P. Héritier, Gamma double prime precipitation kinetic in Alloy 718, Mater. Sci. Eng. A 486 (2008) 117–122, https://doi.org/10.1016/j.msea.2007.08.046.
[21] Y. Han, P. Deb, M.C. Chaturvedi, Coarsening behaviour of γ′′- and γ′-particles in Inconel alloy 718, Met. Sci. 16 (1982) 555–562, https://doi.org/10.1179/030634582790427118.
[22] N.H. Fletcher, Size effect in heterogeneous nucleation, J. Chem. Phys. 29 (1958) 572–576.
[23] N.H. Fletcher, Nucleation by crystalline particles, J. Chem. Phys. 38 (1963) 237–240.
[24] J.W. Cahn, J.E. Hilliard, Free energy of a nonuniform system. I. Interfacial free energy, J. Chem. Phys. 28 (1958) 258–267.
[25] S.M. Allen, J.W. Cahn, Ground state structures in ordered binary alloys with second neighbor interactions, Acta Metall. 20 (1972) 423–433, https://doi.org/10.1016/0001-6160(72)90037-5.
[26] Y. Wang, L.-Q. Chen, A. Khachaturyan, Computer simulation of microstructure evolution in coherent solids, PTM'94, Solid Solid Phase Transform. (1994) 245–265.
[27] Y.H. Wen, Y. Wang, L.A. Bendersky, L.Q. Chen, Microstructural evolution during the α2→α2+O transformation in Ti–Al–Nb alloys: phase-field simulation and experimental validation, Acta Mater. 48 (2000) 4125–4135, https://doi.org/10.1016/S1359-6454(00)00186-5.
[28] H.I. Aaronson, Lectures on the theory of phase transformations, TMS, Warrendale, Pa, 1999, 2. ed.
[29] C. Zener, Theory of growth of spherical precipitates from solid solution, J. Appl. Phys. 20 (1949) 950–953, https://doi.org/10.1063/1.1698258.
[30] P.J. Phillips, D. McAllister, Y. Gao, D. Lv, R.E.A. Williams, B. Peterson, Y. Wang, M. J. Mills, Nano γ′/γ ″ composite precipitates in Alloy 718, Appl. Phys. Lett. 100 (2012), 211913, https://doi.org/10.1063/1.4721456.
[31] S. Kumar Makineni, S. Sugathan, S. Meher, R. Banerjee, S. Bhattacharya, S. Kumar, K. Chattopadhyay, Enhancing elevated temperature strength of copper containing aluminium alloys by forming L12 Al3Zr precipitates and nucleating θ″ precipitates on them, Sci. Rep. 7 (2017) 11154, https://doi.org/10.1038/s41598-017-11540-2.
[32] B. Bhadak, R.K. Singh, A. Choudhury, Equilibrium multi-precipitate configurations, Metall. Mater. Trans. A 51 (2020) 5414–5431, https://doi.org/10.1007/s11661-020-05903-0.
[33] D.P. McAllister, Shearing Mechanisms and Complex Particle Growth in Nickel Superalloy 718, The Ohio State University, 2016. http://rave.ohiolink.edu/etdc/view?acc_num=osu1461079188.